



# Nonlinear Vibration Analysis of Beam Microgyroscopes using Nonlocal Strain Gradient Theory

Moeen Radgolchin<sup>1</sup> · Masoud Tahani<sup>1</sup>

Received: 14 August 2020 / Revised: 22 January 2021 / Accepted: 5 February 2021

© The Author(s), under exclusive licence to Springer Science+Business Media, LLC part of Springer Nature 2021

## Abstract

The objective of this paper is to present a novel nonlocal strain gradient formulation for dynamic analysis of microgyroscopes. Taking into account the effect of nonlocal and gradient strains, the coupled equations of motion and the corresponding boundary conditions are derived using the Hamilton's principle. Reduced order models for electrostatic and electrodynamic performance of the gyroscope are presented based on Galerkin projection technique. First, the influence of nonlocal and length-scale parameters on the electrostatic instability of the microgyroscope are investigated and it will be demonstrated that for electrostatic loading, the pull-in instability is delayed with decreasing the nonlocal and/or increasing the length-scale parameters. Then the equations governing the electrodynamic performance of the system are solved and the time responses and phase diagrams along to the drive and sense directions are presented. The stable amplitude and instability margin of the gyroscope under electrodynamic loading will be demonstrated to be subjected to nonlocal and length-scale parameters. Finally the frequency response of the gyroscope along the sense and drive directions are scrutinized. Accordingly, it will be shown that the nonlocal and length-scale values affect the near-resonance amplitude of vibration significantly. Furthermore, altering the values of nonlocal and length-scale parameters can change the distance between two peak frequencies as well as their absolute values.

**Keywords** Microgyroscope · Nonlocal and length-scale parameters · Electrostatic and electrodynamic response · Frequency response · Dynamic amplification

---

✉ Masoud Tahani  
mtahani@um.ac.ir

Moeen Radgolchin  
moeen.radgolchin@mail.um.ac.ir

<sup>1</sup> Department of Mechanical Engineering, Ferdowsi University of Mashhad, Mashhad, Iran

## 1 Introduction

Microelectromechanical gyroscopes have found numerous applications such as in inertial navigations, automotive engineering, virtual reality, robotics, video camera stabilization and many other instances [1–10]. Among various categories of microgyroscopes, suspended vibratory gyroscopes are of special importance thanks to suitability for fabrication using micromachining processes. Micromachined beam gyroscopes comprise an oscillating mass suspended over an elastic beam. When the gyroscope body vibrates along the lateral axis (named drive direction) in a rotational frame, the Coriolis effect gives rise to a secondary oscillation perpendicular to the primary one (called the sense direction) with an amplitude proportional to the rotational velocity. Consequently, the rate of angular velocity can be measured via sensing the secondary oscillatory motion.

Beam microgyroscopes are excited via electrostatic, electromagnetic or piezoelectric actuation schemes along the drive direction. The sensing procedure along the sense direction can also be accomplished using electrostatic, electromagnetic, piezoelectric, optical, capacitive, or piezoresistive principles. Fast response and simplicity of electrostatic actuation makes it preferable for both drive and sense applications [11]. However, there would be an upper limit for electrical actuation due to pull-in instability. Accordingly, pull-in phenomenon has been extensively investigated in prior arts [12–21].

Studying small-scale structures entails incorporating special features into the mathematical model which cannot be provided using classical approaches. Size-dependent behavior is among the most remarkable characteristics that was observed in micron and sub-micron structures [22]. Accordingly, higher-order continuum theories were presented to improve the accuracy of analytical modeling and capture the size dependent behavior of microstructures. The nonlocal and strain gradient theories are two prominent higher-order approaches that have drawn considerable attention during recent years.

The nonlocal elasticity theory, proposed by Eringen and Edelen [23] and Eringen [24], assumes the stress at a certain point of an elastic body as a function of strains at all points in the continuum. In recent years several studies have been dedicated to investigate the behavior of small-scale structures in the context of nonlocal elasticity theory. In the area of beam structures, Reddy and El-Borgi [25], formulated the problem of Euler–Bernoulli and Timoshenko microbeams for the case of moderate rotations using nonlocal elasticity theory which were then solved using a nonlinear finite element model. Rahmani and Pedram [26], investigated dynamics of thick nanobeams made of functionally graded materials based on the nonlocal elasticity. Najar et al. [27] studied the small scale effect on the nonlinear static and dynamic response of a capacitive nanoactuators subjected to a DC voltage. They included the effect of residual stresses, initial deflection, von-Kármán nonlinear strains and intermolecular forces such as the Casimir and von der Waals in their model. Kivi et al. [28] investigated the bifurcation of nano-beams utilizing nonlocal elasticity. Ebrahimi and Salari [29, 30] modelled thermal buckling and vibration analysis of functionally graded nanobeams using

nonlocal elasticity approach. Nejad et al. [31] presented a solution for the buckling problem of Euler–Bernoulli nano-scale beams made of two-directional functionally graded materials. The nonlocal elasticity has also been employed to study post buckling vibration analysis of piezoelectric Timoshenko nanobeams [32]. In this study, the beam was considered under axial compression force, an applied voltage and a uniform temperature change and the generalized quadrature method was utilized to solve the resulted equations.

On the other hand, the strain gradient theory describes the potential energy of a continuum as a function of strain tensor and its gradients. Primary form of the gradient theory was formulated by Mindlin and Tiersten [33], Aifantis [34] and Toupin [35] in which four size-dependent constants were added to the constitutive equations. Lam et al. [36] modified the initial formulation and presented a more compact format which included three additional length-scale parameter to the strain energy of a deformable body. As a result, the size effect can be acceptably captured in the mathematical model and the conformity of analytical predications and experimental findings is be improved remarkably. Accordingly, the strain gradient theory has been extensively utilized to study the mechanical behavior of micro structures. As some examples, static and vibration analysis of Euler–Bernoulli [37, 38], Timoshenko [39–41], third-order shear deformable [42] and Reddy–Levinson beam [43], non-linear large deformation [44], pre-deformed [45] and curved microbeams [46], functionally graded [47, 48], viscoelastic [49, 50], piezoelectric microbeams [51–53], thermal analysis [54], free and forced vibration [38, 55] and buckling analysis of beams in micro-scale [56, 57], carbon nanotubes [58], pull-in instability of microbeams [59] and random vibration analysis of piezoelectric microbeams [60] as well as many other examples witness the superiority of strain gradient theory in providing accurate predictions for micro/nano structure modelling.

Application of the nonlocal elasticity to some problems leads to paradoxes. For example, in bending analysis of the Euler–Bernoulli cantilever nanobeams subjected to a point load, the results of nonlocal and classical theories are identical [61, 62]. Furthermore, the nonlocal elasticity can only capture the softening effect while stiffness enhancement is also reported experimentally in the existed literature [36, 63]. The strain gradient theory on the other hand incorporates the stiffening effect into its formulation [60, 64]. This implies that the nonlocal and strain gradient formulations define two different size dependent behaviors. Accordingly, the two theories was combined into a compact theory called *nonlocal strain gradient theory* by the work of Lim et al. [65] in order to establish a more comprehensive framework for micro systems analysis. According to this new formulation, the stress at any point of a continuum is a function of non-gradient nonlocal and higher-order strain gradient stress fields. In this regard, two additional higher-order parameters, one capturing the non-local and one accounting for the gradient stress field, are incorporated into the constitutive equations. It was shown that for beam structures, the results of nonlocal strain gradient theory are in excellent accordance with that of molecular dynamic simulations. Consequently, the mechanical behavior of micro/nano-structures have been re-examined using the nonlocal strain gradient theory. To mention some of available arts, Li and Hu [66] investigated size dependent effects on the post-buckling behaviors of nonlinear Euler–Bernoulli beams and dependence of buckling load

on the nonlocal and length-scale parameters. Şimşek [67] presented a nonlinear free vibration analysis of a functionally graded nanobeams using the nonlocal strain gradient theory. Bending and free vibration analysis of nonlocal strain gradient functionally graded (FG) beams was investigated by Li and Hu [68] and Fang et al. [69] respectively. Li et al. [70] proposed a nonlocal strain gradient model for longitudinal vibration of nano-rods. Ebrahimi and Barati [71] analyzed buckling problem of size-dependent shear-deformable curved FG nanobeams using the concept of nonlocal strain gradient theory. Xu et al. [72] formulated the buckling of elastic beams by means of the nonlocal strain gradient approach. Farajpour et al. [73] studied the effects of the nonlocal and material length scale parameters on the buckling behavior of orthotropic nanoplates using the nonlocal strain gradient theory.

The abovementioned review reveals that the nonlocal strain gradient theory has been successfully employed in formulating the mechanical behavior of miniaturized systems and continues to spread through different micro/nano devices analysis. Nevertheless, as far as the authors know, electromechanical performance of microgyroscopes based on the nonlocal strain gradient theory has not been addressed yet. Accordingly, this paper presents a new nonlinear dynamic model for doubly-clamped microgyroscopes in the context of nonlocal strain gradient theory. The major novel contributions of this paper are: (1) develop a nonlocal strain gradient model for doubly-clamped microgyroscopes for the first time and (2) demonstrate and investigate the influence of nonlocal and length-scale parameters on the electrostatic, stability and electrodynamic response of the gyroscope which were not considered in previous related arts.

## 2 Nonlocal Strain Gradient Theory

According to the nonlocal strain gradient theory, the strain energy of a linear elastic isotropic continuum is defined as [65]

$$U = \frac{1}{2} \int_V \left( \sigma_{ij} \epsilon_{ij} + \sigma_{ij}^{(1)} \nabla \epsilon_{ij} \right) dV \quad (1)$$

In this equation  $\epsilon_{ij}$  is the classical strain. Also  $\sigma_{ij}$  and  $\sigma_{ij}^{(1)}$  are the nonlocal stress and higher-order nonlocal stress tensors defined as

$$\sigma_{ij} = C_{ijkl} \int_V \alpha_0(|x - x'|, e_0 a) \epsilon'_{kl} dV \quad (2)$$

$$\sigma_{ij}^{(1)} = l_m^2 C_{ijkl} \int_V \alpha_1(|x - x'|, e_1 a) \nabla \epsilon'_{kl} dV \quad (3)$$

In Eqs. (2) and (3),  $C_{ijkl}$  are elements of fourth-order elasticity tensor,  $l_m$  is the material length-scale parameter taking the significance of strain gradient stress field into consideration and  $e_0 a$  and  $e_1 a$  are nonlocal parameters representing the effect

of nonlocal elastic stress field. In addition,  $\alpha_0(|x - x'|, e_0 a)$  and  $\alpha_1(|x - x'|, e_1 a)$  are nonlocal functions corresponding to classical and strain gradient stress tensors, respectively. The total stress tensor, which includes both nonlocal and strain gradient stress tensors is then expressed as

$$t_{ij} = \sigma_{ij} - \nabla \sigma_{ij,m}^{(1)} \quad (4)$$

in which  $\nabla = \partial/\partial x$  is the nabla operator.

Considering  $e_0 = e_1 = e$  and supposing that the nonlocal functions satisfy the conditions given in [24] one can say

$$[1 - (ea)^2 \nabla^2] \sigma_{ij} = C_{ijkl} \varepsilon_{kl} \quad (5)$$

$$[1 - (ea)^2 \nabla^2] \sigma_{ij}^{(1)} = l_m^2 C_{ijkl} \nabla \varepsilon_{kl} \quad (6)$$

For one-dimensional structures such as beams,  $\varepsilon_{xx}$  would be the only nonzero strain element and  $\nabla^2$  is the Laplacian operator. Consequently, the general constitutive equation corresponding to nonlocal strain gradient theory becomes [67]:

$$[1 - (ea)^2 \nabla^2] t_{xx} = E(1 - l_m^2 \nabla^2) \varepsilon_{xx} \quad (7)$$

### 3 Mathematical Modelling

Schematic view of a micro-gyroscope with length  $L$ , width  $b$  and thickness  $h$  clamped at both extremes and rotating at  $\hat{\Omega}$  along its longitudinal axis is shown in Fig. 1. A concentrated mass  $M$  is attached at its middle point on which the electrical actuation forces are applied. The sense and drive directions are denoted as  $\hat{z}$  and  $\hat{y}$ , respectively.

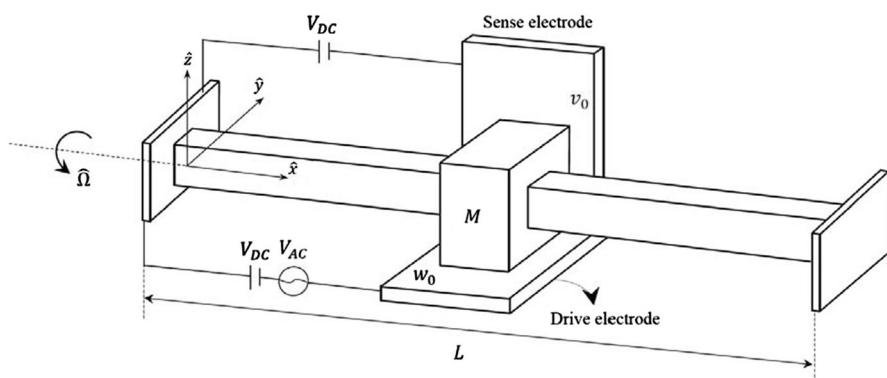


Fig. 1 Schematic view of a doubly-clamped microgyroscope

The displacement field of the gyroscope subjected to coupled lateral-transverse loads can be defined using the Euler–Bernoulli beam theory as

$$u_1 = \hat{u} - z \frac{\partial \hat{w}}{\partial \hat{x}} - y \frac{\partial \hat{v}}{\partial \hat{x}}, \quad u_2 = \hat{v}, \quad u_3 = \hat{w} \quad (8)$$

where  $\hat{u}$ ,  $\hat{v}$  and  $\hat{w}$  are axial, lateral and transverse deflections of the beam and  $u_1$ ,  $u_2$  and  $u_3$  are total displacement of a material point of the beam fibers along  $\hat{x}$ ,  $\hat{y}$  and  $\hat{z}$  directions, respectively. Therefore, the nonzero strain component can be obtained using the von-Kármán relation as [74]

$$\epsilon_{xx} = \frac{\partial \hat{u}}{\partial \hat{x}} - z \frac{\partial^2 \hat{w}}{\partial \hat{x}^2} - y \frac{\partial^2 \hat{v}}{\partial \hat{x}^2} + \frac{1}{2} \left( \frac{\partial \hat{v}}{\partial \hat{x}} \right)^2 + \frac{1}{2} \left( \frac{\partial \hat{w}}{\partial \hat{x}} \right)^2 \quad (9)$$

which gives the nonzero stress component as

$$\sigma_{xx} = E \left[ \frac{\partial \hat{u}}{\partial \hat{x}} - z \frac{\partial^2 \hat{w}}{\partial \hat{x}^2} - y \frac{\partial^2 \hat{v}}{\partial \hat{x}^2} + \frac{1}{2} \left( \frac{\partial \hat{v}}{\partial \hat{x}} \right)^2 + \frac{1}{2} \left( \frac{\partial \hat{w}}{\partial \hat{x}} \right)^2 \right] \quad (10)$$

Simplifying the second term of the strain energy variation in Eq. (1) using integration by-part, one can get

$$\delta U = \int_V (\sigma_{xx} \delta \epsilon_{xx} - \nabla \sigma_{xx}^{(1)} \delta \epsilon_{xx}) dV + \left[ \int_A \sigma_{xx}^{(1)} \delta \epsilon_{xx} dA \right]_0^L = \int_V t_{xx} \delta \epsilon_{xx} dV + \left[ \int_A \sigma_{xx}^{(1)} \delta \epsilon_{xx} dA \right]_0^L \quad (11)$$

Defining the following classical and nonlocal stress resultants

$$\begin{aligned} (N_c, M_c^{(z)}, M_c^{(y)}) &= \int_A (1, \hat{z}, \hat{y}) t_{xx} dA \\ (N_{nc}, M_{nc}^{(z)}, M_{nc}^{(y)}) &= \int_A (1, \hat{z}, \hat{y}) \sigma_{xx}^{(1)} dA \end{aligned} \quad (12)$$

Equation (11) is further simplified to

$$\begin{aligned} \delta U = & - \int_0^L \left( \frac{\partial N_c}{\partial \hat{x}} \delta \hat{u} + \frac{\partial}{\partial \hat{x}} \left( N_c \frac{\partial \hat{v}}{\partial \hat{x}} \right) \delta \hat{v} + \frac{\partial}{\partial \hat{x}} \left( N_c \frac{\partial \hat{w}}{\partial \hat{x}} \right) \delta \hat{w} + \frac{\partial^2 M_c^{(z)}}{\partial \hat{x}^2} \delta \hat{w} + \frac{\partial^2 M_c^{(y)}}{\partial \hat{x}^2} \delta \hat{v} \right) d\hat{x} \\ & + \left\{ N_c \frac{\partial \hat{v}}{\partial \hat{x}} \delta \hat{v} + N_c \frac{\partial \hat{w}}{\partial \hat{x}} \delta \hat{w} - \left( M_c^{(z)} \frac{\partial \delta \hat{w}}{\partial \hat{x}} - \frac{\partial M_c^{(z)}}{\partial \hat{x}} \delta \hat{w} \right) + N_c \delta \hat{u} - \left( M_c^{(y)} \frac{\partial \delta \hat{v}}{\partial \hat{x}} - \frac{\partial M_c^{(y)}}{\partial \hat{x}} \delta \hat{v} \right) \right. \\ & \left. + N_{nc} \left( \frac{\partial \delta \hat{u}}{\partial \hat{x}} + \frac{\partial \delta \hat{v}}{\partial \hat{x}} \frac{\partial \hat{v}}{\partial \hat{x}} + \frac{\partial \delta \hat{w}}{\partial \hat{x}} \frac{\partial \hat{w}}{\partial \hat{x}} \right) - \left( M_{nc}^{(z)} \left( \frac{\partial^2 \delta \hat{w}}{\partial \hat{x}^2} \right) + M_{nc}^{(y)} \left( \frac{\partial^2 \delta \hat{v}}{\partial \hat{x}^2} \right) \right) \right\} \Big|_0^L \end{aligned} \quad (13)$$

The kinetic energy of the gyroscope can be decomposed into translational and rotational parts. Defining an inertial reference frame  $C(\hat{x}\hat{y}\hat{z})$  and a rotational

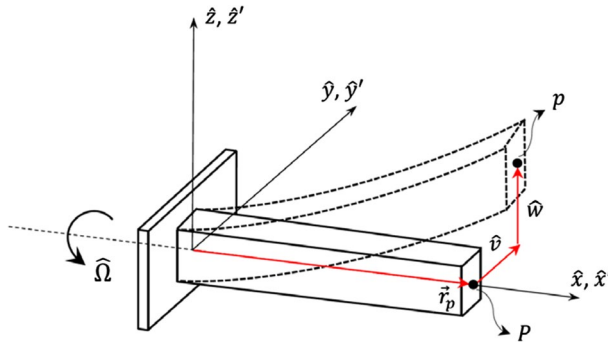


**Fig. 2** Displacement components of a generic point of the microgyroscope

frame  $C'(\hat{x}'\hat{y}'\hat{z}')$ , the displacement components of a generic point  $P$  when moving to the deflected position  $P'$  can be described as (see Fig. 2)

$$\vec{R} = r_p \vec{i} + \hat{v} \vec{j} + \hat{w} \vec{k} \quad (14)$$

Accordingly, the velocity of a point in the deformed state can be described as

$$\left( \frac{d\vec{R}}{dt} \right)_c = \left( \frac{d\vec{R}}{dt} \right)_{c'} + \hat{\Omega} \times \vec{R} = \left( \frac{\partial \hat{v}}{\partial t} - \hat{w} \hat{\Omega} \right) + \left( \frac{\partial \hat{w}}{\partial t} + \hat{v} \hat{\Omega} \right) \quad (15)$$

Using Eq. (15), the translational kinetic energy of the beam is expressed as

$$T_T = \frac{1}{2} \int_0^L \left\{ (\rho A + M \delta(\hat{x} - L/2)) \left[ \left( \frac{\partial \hat{w}}{\partial t} \right)^2 + \left( \frac{\partial \hat{v}}{\partial t} \right)^2 + \hat{\Omega}^2 (\hat{w}^2 + \hat{v}^2) + 2\hat{\Omega} \left( \hat{v} \frac{\partial \hat{w}}{\partial t} - \hat{w} \frac{\partial \hat{v}}{\partial t} \right) \right] \right\} d\hat{x} \quad (16)$$

where  $\delta$  denotes the Dirac delta function.

To determine the rotational kinetic energy, two other reference frames are defined which account for rotation of the beam cross section about coordinate axes. Reference frame  $D(x_1 y_1 z_1)$  with unit vectors  $(\vec{i}_1, \vec{j}_1, \vec{k}_1)$  is considered as a result of rotating frame  $C'$  by angle  $\phi$  about  $\hat{z}'$ . The fourth reference frame is called  $D'(x'_1 y'_1 z'_1)$  with unit vector  $(\vec{i}'_1, \vec{j}'_1, \vec{k}'_1)$  and is obtained by rotating frame  $D$  with angle  $\psi$  about  $y_1$  axis. Therefore, the angular velocity of the microgyroscope is stated in terms of  $D'$  unit vectors as

$${}^c \vec{\Omega}^{D'} = \left( \hat{\Omega} \cos \psi \cos \phi - \frac{\partial \phi}{\partial t} \sin \psi \right) \vec{i}'_1 + \left( \frac{\partial \phi}{\partial t} - \hat{\Omega} \sin \phi \right) \vec{j}'_1 + \left( \hat{\Omega} \sin \psi \cos \phi + \frac{\partial \phi}{\partial t} \cos \psi \right) \vec{k}'_1 \quad (17)$$

Now replacing the small rotation angles as  $\phi = \partial v / \partial x$  and  $\psi = -\partial w / \partial x$ , the rotational kinetic energy of the gyroscope is resulted as

$$T_R = \frac{1}{2} \int_0^L \left\{ J \left( \left( \frac{\partial^2 \hat{w}}{\partial \hat{x} \partial \hat{t}} \right)^2 + \left( \frac{\partial^2 \hat{v}}{\partial \hat{x} \partial \hat{t}} \right)^2 \right) + J \hat{\Omega}^2 \left( \left( \frac{\partial \hat{w}}{\partial \hat{x}} \right)^2 + \left( \frac{\partial \hat{v}}{\partial \hat{x}} \right)^2 \right) + 2J \hat{\Omega} \left( \frac{\partial \hat{v}}{\partial \hat{x}} \frac{\partial^2 \hat{w}}{\partial \hat{x} \partial \hat{t}} + \frac{\partial \hat{w}}{\partial \hat{x}} \frac{\partial^2 \hat{v}}{\partial \hat{x} \partial \hat{t}} \right) \right\} d\hat{x} + LJ\hat{\Omega}^2 \quad (18)$$

It has to be noted that in Eq. (18), the assumption of  $J_{x'_1} = J_{y'_1} = J_{z'_1} = J$  is employed. The total kinetic energy of the gyroscope is then expressed as  $T = T_T + T_R$ . Finally, variation of the works done by external loads including electrical actuation in the transverse and lateral directions as well as a distributed visco-damping are written as

$$\delta W_{ext} = \int_0^L \delta \left( \hat{x} - \frac{L}{2} \right) \frac{\epsilon A_v V_{DC}^2}{2(v_0 - \hat{v}(x, t))^2} \delta \hat{v} d\hat{x} + \int_0^L \delta \left( \hat{x} - \frac{L}{2} \right) \frac{\epsilon A_w (V_{DC} + V_{AC} \cos(\hat{\Omega}_e \hat{t}))^2}{2(w_0 - \hat{w}(x, t))^2} \delta \hat{w} d\hat{x} - c \int_0^L \left( \frac{\partial \hat{w}}{\partial \hat{t}} \delta \hat{w} + \frac{\partial \hat{v}}{\partial \hat{t}} \delta \hat{v} \right) d\hat{x} \quad (19)$$

where  $\epsilon$  is the dielectric constant of the gap medium and  $w_0$  and  $v_0$  (as shown in Fig. 1) are the gap distances of the drive and sense capacitors, respectively. Moreover,  $A_w$  and  $A_v$  denote the areas of the drive and sense capacitors, respectively.

Employing the Hamilton's principle as follows,

$$\int_{t_1}^{t_2} \delta(U - T - W) = 0 \quad (20)$$

equations governing the dynamic behavior of the system are resulted as

$$I \frac{\partial^2 \hat{u}}{\partial \hat{t}^2} + \frac{\partial N_c}{\partial \hat{x}} = 0 \quad (21)$$

$$\begin{aligned} \frac{\partial}{\partial \hat{x}} \left( N_c \frac{\partial \hat{v}}{\partial \hat{x}} \right) + \frac{\partial^2 M_c^{(y)}}{\partial \hat{x}^2} + \left( \rho A + M \delta \left( \hat{x} - \frac{L}{2} \right) \right) \left( \frac{\partial^2 \hat{v}}{\partial \hat{t}^2} - \hat{\Omega}^2 \hat{v} - 2\hat{\Omega} \frac{\partial \hat{w}}{\partial \hat{t}} - \hat{w} \dot{\hat{\Omega}} \right) \\ + J \left( \hat{\Omega}^2 \frac{\partial^2 \hat{v}}{\partial \hat{x}^2} - \frac{\partial^4 \hat{v}}{\partial \hat{x}^2 \partial \hat{t}^2} - \dot{\hat{\Omega}} \frac{\partial^2 \hat{w}}{\partial \hat{x}^2} \right) = \delta \left( \hat{x} - \frac{L}{2} \right) \frac{\epsilon A_v V_{DC}^2}{2(v_0 - \hat{v})^2} \end{aligned} \quad (22)$$

$$\begin{aligned} \frac{\partial}{\partial \hat{x}} \left( N_c \frac{\partial \hat{w}}{\partial \hat{x}} \right) + \frac{\partial^2 M_c^{(z)}}{\partial \hat{x}^2} + \left( \rho A + M \delta \left( \hat{x} - \frac{L}{2} \right) \right) \left( \frac{\partial^2 \hat{w}}{\partial \hat{t}^2} - \hat{\Omega}^2 \hat{w} + 2\hat{\Omega} \frac{\partial \hat{v}}{\partial \hat{t}} + \hat{v} \dot{\hat{\Omega}} \right) \\ + J \left( \hat{\Omega}^2 \frac{\partial^2 \hat{w}}{\partial \hat{x}^2} - \frac{\partial^4 \hat{w}}{\partial \hat{x}^2 \partial \hat{t}^2} - \dot{\hat{\Omega}} \frac{\partial^2 \hat{v}}{\partial \hat{x}^2} \right) = \delta \left( \hat{x} - \frac{L}{2} \right) \frac{\epsilon A_w (V_{DC} + V_{AC} \cos(\hat{\Omega}_e \hat{t}))^2}{2(w_0 - \hat{w})^2} \end{aligned} \quad (23)$$



Also, the boundary conditions at  $\hat{x} = 0$  and  $\hat{x} = L$  are briefed in the Appendix I.

Utilizing Eq. (7) and the definition of force and moment resultant given in Eq. (12), the following relations are obtained

$$N_c - (ea)^2 \frac{\partial^2 N_c}{\partial \hat{x}^2} = A_{xx} \left( 1 - l_m^2 \frac{\partial^2}{\partial \hat{x}^2} \right) \left( \frac{\partial \hat{u}}{\partial \hat{x}} + \frac{1}{2} \left( \frac{\partial \hat{v}}{\partial \hat{x}} \right)^2 + \frac{1}{2} \left( \frac{\partial \hat{w}}{\partial \hat{x}} \right)^2 \right) \quad (24)$$

$$M_c^{(z)} - (ea)^2 \frac{\partial^2 M_c^{(z)}}{\partial \hat{x}^2} = -B_{xx}^{(z)} \frac{\partial^2 \hat{w}}{\partial \hat{x}^2} + B_{xx}^{(z)} l_m^2 \frac{\partial^4 \hat{w}}{\partial \hat{x}^4} \quad (25)$$

$$M_c^{(y)} - (ea)^2 \frac{\partial^2 M_c^{(y)}}{\partial \hat{x}^2} = -B_{xx}^{(y)} \frac{\partial^2 \hat{v}}{\partial \hat{x}^2} + B_{xx}^{(y)} l_m^2 \frac{\partial^4 \hat{v}}{\partial \hat{x}^4} \quad (26)$$

in which

$$(A_{xx}, B_{xx}^{(z)}, B_{xx}^{(y)}) = E \int_A (1, \hat{z}^2, \hat{y}^2) dA \quad (27)$$

It has to be noted that in deriving Eqs. (24)–(26), the fact that  $\int_A \hat{y} dA = \int_A \hat{z} dA = 0$  are employed.

Neglecting the axial inertia in Eq. (21) and inserting the outcome into Eq. (24), one can get [67]

$$N_c = A_{xx} \left( 1 - l_m^2 \frac{\partial^2}{\partial \hat{x}^2} \right) \left( \frac{\partial \hat{u}}{\partial \hat{x}} + \frac{1}{2} \left( \frac{\partial \hat{v}}{\partial \hat{x}} \right)^2 + \frac{1}{2} \left( \frac{\partial \hat{w}}{\partial \hat{x}} \right)^2 \right) \quad (28)$$

which assuming  $\partial N_c / \partial \hat{x} = 0$  leads to

$$\left( 1 - l_m^2 \frac{\partial^2}{\partial \hat{x}^2} \right) \left( \frac{\partial \hat{u}}{\partial \hat{x}} + \frac{1}{2} \left( \frac{\partial \hat{v}}{\partial \hat{x}} \right)^2 + \frac{1}{2} \left( \frac{\partial \hat{w}}{\partial \hat{x}} \right)^2 \right) = \frac{C}{A_{xx}} \quad (29)$$

In this equation,  $C$  is the integration constant. Integrating Eq. (29) over the microbeam length and using the boundary conditions fixed ends  $\hat{u}(0) = \hat{u}(L) = \frac{\partial^2 \hat{u}}{\partial \hat{x}^2}(0) = \frac{\partial^2 \hat{u}}{\partial \hat{x}^2}(L) = 0$  for the fixed ends, the axial force  $N_c$  is derived as [75]

$$N_c = \frac{A_{xx}}{2L} \left( 1 - l_m^2 \frac{\partial^2}{\partial \hat{x}^2} \right) \int_0^L \left( \left( \frac{\partial \hat{v}}{\partial \hat{x}} \right)^2 + \left( \frac{\partial \hat{w}}{\partial \hat{x}} \right)^2 \right) d\hat{x} \quad (30)$$

Now substituting  $N_c$ ,  $M_c^{(z)}$  and  $M_c^{(y)}$  from Eqs. (30), (25) and (26) into Eqs. (22) and (23), equations of motion take the form

$$\begin{aligned}
& \frac{A_{xx}}{2L} \left( 1 - l_m^2 \frac{\partial^2}{\partial \hat{x}^2} \right) \left\{ \int_0^L \left( \left( \frac{\partial \hat{v}}{\partial \hat{x}} \right)^2 + \left( \frac{\partial \hat{w}}{\partial \hat{x}} \right)^2 \right) d\hat{x} \right\} \left( \frac{\partial^2 \hat{v}}{\partial \hat{x}^2} - (ea)^2 \frac{\partial^4 \hat{v}}{\partial \hat{x}^4} \right) \\
& + \frac{\partial^2}{\partial \hat{x}^2} \left( B_{xx}^{(y)} \frac{\partial^2 \hat{v}}{\partial \hat{x}^2} - B_{xx}^{(y)} l_m^2 \frac{\partial^4 \hat{v}}{\partial \hat{x}^4} \right) = (1 - (ea)^2 \nabla^2) \left\{ \delta \left( \hat{x} - \frac{L}{2} \right) \frac{\epsilon A_y V_{DC}^2}{2(v_0 - \hat{v})^2} \right. \\
& \left. - \left( \rho A + M \delta \left( \hat{x} - \frac{L}{2} \right) \right) \left( \frac{\partial^2 \hat{v}}{\partial \hat{t}^2} - \hat{\Omega}^2 \hat{v} - 2\hat{\Omega} \frac{\partial \hat{w}}{\partial \hat{t}} - \hat{w} \dot{\hat{\Omega}} \right) - J \left( \hat{\Omega}^2 \frac{\partial^2 \hat{v}}{\partial \hat{x}^2} - \frac{\partial^4 \hat{v}}{\partial \hat{x}^2 \partial \hat{t}^2} - \dot{\hat{\Omega}} \frac{\partial^2 \hat{w}}{\partial \hat{x}^2} \right) \right\} \quad (31)
\end{aligned}$$

$$\begin{aligned}
& \frac{A_{xx}}{2L} \left( 1 - l_m^2 \frac{\partial^2}{\partial \hat{x}^2} \right) \left\{ \int_0^L \left( \left( \frac{\partial \hat{v}}{\partial \hat{x}} \right)^2 + \left( \frac{\partial \hat{w}}{\partial \hat{x}} \right)^2 \right) d\hat{x} \right\} \left( \frac{\partial^2 \hat{w}}{\partial \hat{x}^2} - (ea)^2 \frac{\partial^4 \hat{w}}{\partial \hat{x}^4} \right) \\
& + \frac{\partial^2}{\partial \hat{x}^2} \left( B_{xx}^{(z)} \frac{\partial^2 \hat{w}}{\partial \hat{x}^2} - B_{xx}^{(z)} l_m^2 \frac{\partial^4 \hat{w}}{\partial \hat{x}^4} \right) = (1 - (ea)^2 \nabla^2) \left\{ \delta \left( \hat{x} - \frac{L}{2} \right) \frac{\epsilon A_z (V_{DC} + V_{AC} \cos(\hat{\Omega}_e \hat{t}))^2}{2(w_0 - \hat{w})^2} \right. \\
& \left. - \left( \rho A + M \delta \left( \hat{x} - \frac{L}{2} \right) \right) \left( \frac{\partial^2 \hat{w}}{\partial \hat{t}^2} - \hat{\Omega}^2 \hat{w} + 2\hat{\Omega} \frac{\partial \hat{v}}{\partial \hat{t}} + \hat{v} \dot{\hat{\Omega}} \right) - J \left( \hat{\Omega}^2 \frac{\partial^2 \hat{w}}{\partial \hat{x}^2} - \frac{\partial^4 \hat{w}}{\partial \hat{x}^2 \partial \hat{t}^2} - \dot{\hat{\Omega}} \frac{\partial^2 \hat{v}}{\partial \hat{x}^2} \right) \right\} \quad (32)
\end{aligned}$$

Defining the following normalized variables

$$x = \frac{\hat{x}}{L}, \quad v = \frac{\hat{v}}{v_0}, \quad w = \frac{\hat{w}}{w_0}, \quad t = T\hat{t}, \quad T = \sqrt{\frac{B_{xx}^{(z)}}{\rho AL^4}} \quad (33)$$

the normalized equations of motion become

$$\begin{aligned}
& \frac{A_{xx} v_0^2}{2B_{xx}^{(z)}} \left( 1 - l_m^2 \frac{\partial^2}{\partial x^2} \right) \left\{ \int_0^L \frac{\partial^2}{\partial x^2} \left( \left( \frac{\partial v}{\partial x} \right)^2 + \frac{w_0^2}{v_0^2} \left( \frac{\partial w}{\partial x} \right)^2 \right) dx \right\} \left( \frac{\partial^2 v}{\partial x^2} - \frac{(ea)^2}{L^2} \frac{\partial^4 v}{\partial x^4} \right) + \frac{B_{xx}^{(y)}}{B_{xx}^{(z)}} \left( \frac{\partial^4 v}{\partial x^4} - \frac{l_m^2}{L^2} \frac{\partial^6 v}{\partial x^6} \right) \\
& = \left( 1 - \frac{(ea)^2}{L^2} \nabla^2 \right) \left\{ - \left( 1 + m \delta \left( x - \frac{1}{2} \right) \right) \left( \frac{\partial^2 v}{\partial t^2} - \Omega^2 v - \frac{w_0}{v_0} 2\Omega \frac{\partial w}{\partial t} - \frac{w_0}{v_0} w \dot{\Omega} \right) \right. \\
& \left. - J \left( \Omega^2 \frac{\partial^2 v}{\partial x^2} - \frac{\partial^4 v}{\partial x^2 \partial t^2} - \frac{w_0}{v_0} \Omega \frac{\partial^2 w}{\partial x^2} \right) + \delta \left( x - \frac{1}{2} \right) \frac{\beta_v V_{DC}^2}{v_0^2 (1 - v)^2} \right\} \quad (34)
\end{aligned}$$

$$\begin{aligned}
& \frac{A_{xx}v_0^2}{2B_{xx}^{(z)}} \left(1 - l_m^2 \frac{\partial^2}{\partial x^2}\right) \left\{ \int_0^L \left( \left(\frac{\partial v}{\partial x}\right)^2 + \frac{w_0^2}{v_0^2} \left(\frac{\partial w}{\partial x}\right)^2 \right) dx \right\} \left( \frac{\partial^2 w}{\partial x^2} - \frac{(ea)^2}{L^2} \frac{\partial^4 w}{\partial x^4} \right) \\
& + \left( \frac{\partial^4 w}{\partial x^4} - \frac{l_m^2}{L^2} \frac{\partial^6 w}{\partial x^6} \right) = \left(1 - \frac{(ea)^2}{L^2} \nabla^2\right) \left\{ - \left(1 + m\delta \left(x - \frac{1}{2}\right)\right) \left( \frac{\partial^2 w}{\partial t^2} - \Omega^2 w + 2 \frac{v_0}{w_0} \Omega \frac{\partial v}{\partial t} + \frac{v_0}{w_0} v \dot{\Omega} \right) \right. \\
& \left. - J \left( \Omega^2 \frac{\partial^2 w}{\partial x^2} - \frac{\partial^4 w}{\partial x^2 \partial t^2} - \frac{v_0}{w_0} \dot{\Omega} \frac{\partial^2 v}{\partial x^2} \right) + \delta \left(x - \frac{1}{2}\right) \frac{\beta_w \left( V_{DC} + V_{AC} \cos(\hat{\Omega}_e t) \right)^2}{(1-w)^2} \right\}
\end{aligned} \quad (35)$$

where

$$\beta_v = \frac{\varepsilon A_v L^3}{2B_{xx}^{(z)} v_0^3}, \quad \beta_w = \frac{\varepsilon A_w L^3}{2B_{xx}^{(z)} w_0^3}, \quad m = \frac{M}{\rho AL}, \quad j = \frac{J}{\rho AL^2}, \quad \Omega = \frac{\hat{\Omega}}{T}, \quad \Omega_e = \frac{\hat{\Omega}_e}{T} \quad (36)$$

#### 4 Electrostatic Performance of the Microgyroscope

In this section, quasi-static behavior of the microgyroscope is investigated. To this end, the time-dependent terms of the equations of motion (i.e. the expressions including time derivatives) as well as the AC component of the loading must be removed. As a result, equations governing the electrostatic motion of the gyroscope take the form

$$\begin{aligned}
& \frac{A_{xx}v_0^2}{2B_{xx}^{(z)}} \left(1 - l_m^2 \frac{\partial^2}{\partial x^2}\right) \left\{ \int_0^L \frac{\partial^2}{\partial x^2} \left( \left(\frac{\partial v}{\partial x}\right)^2 + \frac{w_0^2}{v_0^2} \left(\frac{\partial w}{\partial x}\right)^2 \right) dx \right\} \left( \frac{\partial^2 v}{\partial x^2} - \frac{(ea)^2}{L^2} \frac{\partial^4 v}{\partial x^4} \right) + \frac{B_{xx}^{(y)}}{B_{xx}^{(z)}} \left( \frac{\partial^4 v}{\partial x^4} - \frac{l_m^2}{L^2} \frac{\partial^6 v}{\partial x^6} \right) \\
& = \left(1 - \frac{(ea)^2}{L^2} \nabla^2\right) \left\{ - \left(1 + m\delta \left(x - \frac{1}{2}\right)\right) (-\Omega^2 v) - J \left( \Omega^2 \frac{\partial^2 v}{\partial x^2} \right) + \delta \left(x - \frac{1}{2}\right) \frac{\beta_v V_{DC}^2}{v_0^2 (1-v)^2} \right\}
\end{aligned} \quad (37)$$

$$\begin{aligned}
& \frac{A_{xx}v_0^2}{2B_{xx}^{(z)}} \left(1 - l_m^2 \frac{\partial^2}{\partial x^2}\right) \left\{ \int_0^L \left( \left(\frac{\partial v}{\partial x}\right)^2 + \frac{w_0^2}{v_0^2} \left(\frac{\partial w}{\partial x}\right)^2 \right) dx \right\} \left( \frac{\partial^2 w}{\partial x^2} - \frac{(ea)^2}{L^2} \frac{\partial^4 w}{\partial x^4} \right) + \left( \frac{\partial^4 w}{\partial x^4} - \frac{l_m^2}{L^2} \frac{\partial^6 w}{\partial x^6} \right) \\
& = \left(1 - \frac{(ea)^2}{L^2} \nabla^2\right) \left\{ - \left(1 + m\delta \left(x - \frac{1}{2}\right)\right) (-\Omega^2 w) - J \left( \Omega^2 \frac{\partial^2 w}{\partial x^2} \right) + \delta \left(x - \frac{1}{2}\right) \frac{\beta_w V_{DC}^2}{(1-w)^2} \right\}
\end{aligned} \quad (38)$$

To obtain the reduced-order model, the deflection components  $v$  and  $w$  are expanded in series form as

$$\begin{aligned}
 v(x) &= \sum_{i=1}^M \phi_i(x) p_i \\
 w(x) &= \sum_{i=1}^N \phi_i(x) q_i
 \end{aligned} \tag{39}$$

where  $\phi_i(x)$  denotes the  $i$ th mode shape of the beam and  $p_i$  and  $q_i$  signify the contribution of each mode in electrostatic response. Substituting Eq. (39) into Eqs. (37) and (38) and performing the Galerkin projection leads to

$$\begin{aligned}
 & \frac{A_{xx} v_0^2}{2B_{xx}^{(z)}} \left( 1 - l_m^2 \frac{\partial^2}{\partial x^2} \right) \left\{ \int_0^L \left( \left( \sum_{i=1}^N \phi_i' p_i \right)^2 + \frac{w_0^2}{v_0^2} \left( \sum_{i=1}^N \phi_i' q_i \right)^2 \right) dx \right\} \left\{ \sum_{i=1}^N \int_0^L \left( \phi_i'' - \frac{(ea)^2}{L^2} \phi_i^{(iv)} \right) \phi_j dx \right\} p_i \\
 & + \frac{B_{xx}^{(v)}}{B_{xx}^{(z)}} \left( \sum_{i=1}^N \int_0^L \left( \phi_i^{(iv)} - \frac{l_m^2}{L^2} \phi_i^{(iv)} \right) \phi_j dx \right) p_i = \left( 1 - \frac{(ea)^2}{L^2} \nabla^2 \right) \cdot \\
 & \left\{ - \left( 1 + m\delta \left( x - \frac{1}{2} \right) \right) \left( \Omega^2 \sum_{i=1}^N \int_0^L (-\phi_i + J\phi_i'') \phi_j dx \right) p_i + \int_0^L \delta \left( x - \frac{1}{2} \right) \frac{\beta_v V_{DC}^2 \phi_j dx}{v_0^2 \left( 1 - \sum_{i=1}^N \phi_i p_i \right)^2} \right\}, \quad j = 1, 2, \dots, M
 \end{aligned} \tag{40}$$

$$\begin{aligned}
 & \frac{A_{xx} v_0^2}{2B_{xx}^{(z)}} \left( 1 - l_m^2 \frac{\partial^2}{\partial x^2} \right) \left\{ \int_0^L \left( \left( \sum_{i=1}^N \phi_i' p_i \right)^2 + \frac{w_0^2}{v_0^2} \left( \sum_{i=1}^N \phi_i' q_i \right)^2 \right) dx \right\} \left\{ \sum_{i=1}^N \int_0^L \left( \phi_i'' - \frac{(ea)^2}{L^2} \phi_i^{(iv)} \right) \phi_j dx \right\} q_i \\
 & + \left( \sum_{i=1}^N \int_0^L \left( \phi_i^{(iv)} - \frac{l_m^2}{L^2} \phi_i^{(iv)} \right) \phi_j dx \right) q_i = \left( 1 - \frac{(ea)^2}{L^2} \nabla^2 \right) \cdot \\
 & \left\{ - \left( 1 + m\delta \left( x - \frac{1}{2} \right) \right) \left( -\Omega^2 \sum_{i=1}^N \int_0^L (\phi_i + J\phi_i''(x)) \phi_j dx \right) q_i + \int_0^L \delta \left( x - \frac{1}{2} \right) \frac{\beta_w V_{DC}^2 \phi_j dx}{\left( 1 - \sum_{i=1}^N \phi_i(x) q_i \right)^2} \right\}, \quad j = 1, 2, \dots, N
 \end{aligned} \tag{41}$$

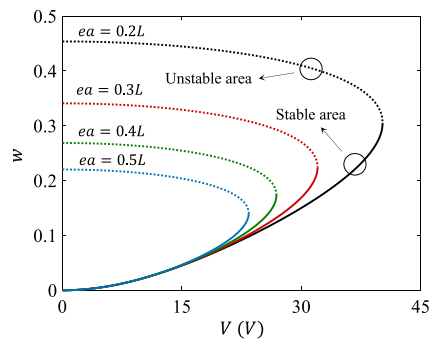
where prime represents  $d/dx$ .

To examine the performance of the system in quasi-static loading regime, a typical microgyroscope with specifications given in Table 1 is considered. The electrostatic response of the gyroscope for different values of nonlocal parameter is depicted in Fig. 3. The solid and dashed lines represent the stable and unstable solutions respectively. The figure reveals that by increasing the parameter  $ea$ , the pull-in instability occurs in smaller values of voltages. Also the maximum achievable amplitude of the gyroscope is further restricted.

The significance of length-scale parameter  $l_m$  in the electrostatic response of the system is highlighted in Fig. 4. This figure demonstrates that as the length-scale parameter is increased, the pull-in phenomenon shifts towards higher voltage values. In other words, employment of materials with higher length-scale values for the gyroscope, can extend the stability margin of the system and increase the instability voltage values.

**Table 1** Geometric and mechanical properties of the gyroscope under study

Parameter	Value
Gyroscope length ( $\mu\text{m}$ )	800
Gyroscope width ( $\mu\text{m}$ )	2.8
Gyroscope thickness ( $\mu\text{m}$ )	2.8
Gap distance ( $\mu\text{m}$ )	2
Electrode area ( $\mu\text{m}^2$ )	392
Middle mass (kg)	$7.2128 \times 10^{-12}$
Young's modulus (GPa)	160
Mass density ( $\text{kg/m}^3$ )	2300

**Fig. 3** Normalized electrostatic response of the microgyroscope for different nonlocal parameters and length-scale value  $l_m = 0.01L$ 

## 5 Electrodynamic Performance of the Microgyroscope

The electrodynamic performance of the microgyroscope is specified when the mid-point mass is subjected to  $(V_{DC} + V_{Ac} \cos \Omega t)$  along the drive direction and  $V_{DC}$  in the sense direction. To derive a reduced order model for the dynamic behavior of the gyroscope, its deflection along the sense and drive directions are stated as

$$\begin{aligned}
 v(x, t) &= \sum_{i=1}^M \phi_i(x) p_i(t) \\
 w(x, t) &= \sum_{i=1}^N \phi_i(x) q_i(t)
 \end{aligned}
 \quad (42)$$

where  $p_i(t)$  and  $q_i(t)$  represent the temporal generalized coordinates capturing the contribution of each mode in the dynamic response. Substituting Eq. (42) into the governing equations in (34) and (35) along with utilizing the Galerkin projection

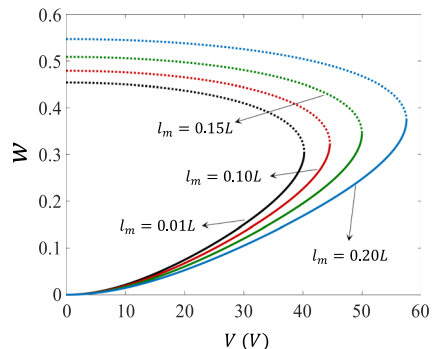
technique along the beam length, the reduced order model corresponding to the electrodynamic operation of the gyroscope is obtained as

$$\begin{aligned}
 & \frac{A_{xx}v_0^2}{2B_{xx}^{(z)}} \left(1 - l_m^2 \frac{\partial^2}{\partial x^2}\right) \left\{ \int_0^L \left( \left( \sum_{i=1}^N \phi_i' p_i \right)^2 + \frac{w_0^2}{v_0^2} \left( \sum_{i=1}^N \phi_i' q_i \right)^2 \right) dx \right\} \left\{ \sum_{i=1}^N \int_0^L \left( \phi_i'' - \frac{(ea)^2}{L^2} \phi_i^{(iv)} \right) \phi_j dx \right\} p_i \\
 & + \frac{B_{xx}^{(y)}}{B_{xx}^{(z)}} \left\{ \sum_{i=1}^N \int_0^L \left( \phi_i^{(iv)} - \frac{l_m^2}{L^2} \phi_i^{(iv)} \right) \phi_j dx \right\} p_i = \left(1 - \frac{(ea)^2}{L^2} \nabla^2\right) \cdot \\
 & \left\{ - \left(1 + m\delta\left(x - \frac{1}{2}\right)\right) \sum_{i=1}^N \int_0^L \phi_i(x) \left( (\ddot{p}_i - \Omega^2 p_i) - \frac{w_0}{v_0} (2\Omega \dot{q}_i - \dot{\Omega} q_i) \right) \phi_j dx \right. \\
 & \left. - J\Omega^2 \sum_{i=1}^N \int_0^L \phi_i''(x) \left( p_i - \dot{p}_i - \frac{w_0}{v_0} \dot{\Omega} q_i \right) \phi_j dx + \int_0^L \delta\left(x - \frac{1}{2}\right) \frac{\beta_v V_{DC}^2 \phi_j dx}{v_0^2 \left(1 - \sum_{i=1}^N \phi_i p_i\right)^2} \right\}, \quad j = 1, 2, \dots, M
 \end{aligned} \quad (43)$$

$$\begin{aligned}
 & \frac{A_{xx}v_0^2}{2B_{xx}^{(z)}} \left(1 - l_m^2 \frac{\partial^2}{\partial x^2}\right) \left\{ \int_0^L \left( \left( \sum_{i=1}^N \phi_i' p_i \right)^2 + \frac{w_0^2}{v_0^2} \left( \sum_{i=1}^N \phi_i' q_i \right)^2 \right) dx \right\} \left\{ \sum_{i=1}^N \int_0^L \left( \phi_i'' - \frac{(ea)^2}{L^2} \phi_i^{(iv)} \right) \phi_j dx \right\} q_i \\
 & + \left\{ \sum_{i=1}^N \int_0^L \left( \phi_i^{(iv)} - \frac{l_m^2}{L^2} \phi_i^{(iv)} \right) \phi_j dx \right\} q_i = \left(1 - \frac{(ea)^2}{L^2} \nabla^2\right) \cdot \\
 & \left\{ - \left(1 + m\delta\left(x - \frac{1}{2}\right)\right) \sum_{i=1}^M \int_0^L \phi_i(x) \left( (\ddot{q}_i - \Omega^2 q_i) + \frac{v_0}{w_0} (2\Omega \dot{p}_i + \dot{\Omega} p_i) \right) \phi_j dx \right. \\
 & \left. - J\Omega^2 \sum_{i=1}^N \int_0^L \phi_i''(x) \left( q_i - \dot{q}_i - \frac{v_0}{w_0} \dot{\Omega} p_i \right) \phi_j dx + \int_0^L \delta\left(x - \frac{1}{2}\right) \frac{\beta_w (V_{DC} + V_{AC} \cos(\Omega_e t))^2 \phi_j dx}{\left(1 - \sum_{i=1}^M \phi_i q_i\right)^2} \right\}, \quad j = 1, 2, \dots, N
 \end{aligned} \quad (44)$$

where prime and dot denote derivative with respect to the normalized variables  $x$  and  $t$ , respectively. Employing  $N = M = 1$  in Eqs. (43) and (44) as it was extensively used in the prior arts [45, 60, 76–78], the resulted equations can be solved

**Fig. 4** Normalized electrostatic response of the microgyro- scope for different length-scale parameters and nonlocal value  $ea = 0.2$



using the fourth-order Runge Kutta method to determine the temporal response of the gyroscope.

## 5.1 Time Response

For the system described in Table 1, the time history response in the sense and drive directions are illustrated in Fig. 5. According to the figure, the response of the beam in both directions is characterized as a combination of a small and a high frequency component. Since the cross section area of the gyroscope and the actuation surface are the same along the sense and drive directions, these two frequencies are similar. Additionally,  $\pi/2$  phase difference exists between the time response in the sense and drive directions.

To further scrutinize the time response of the system, the phase trajectories of the gyroscope in a longer time interval are portrayed in Fig. 6. As the figure shows, starting from specific initial conditions (which is zero in the presented diagram), the amplitude of vibration increases until it reaches a limit cycles which demonstrate that the time response of the gyroscope is stable.

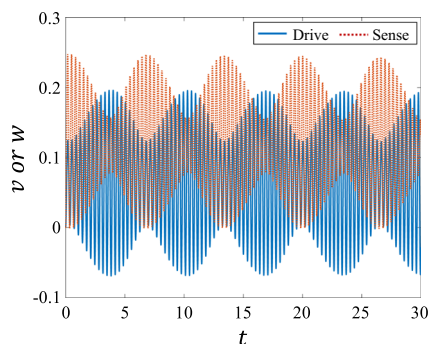
The influence of DC voltage on the temporal response of the gyroscope is illustrated in Fig. 7. According to the figure, increasing the DC voltage changes the displacement components as well as their time derivatives along the sense and drive directions to larger values. As long as the input voltage remains within the operational stability limit, the trajectory maintains its closed nature which is an indication of stable performance. However, if  $V_{DC}$  exceeds a specific value of 16.8V (denoted as dynamic pull-in voltage), the beam becomes unstable and collapse onto the fixed electrodes. In such circumstance, the phase trajectory do not follow a stable closed path.

The dependence of vibration along the drive direction on the AC voltage is also highlighted in Fig. 8. Similar to the previous diagram, for some AC voltages within the stabile zone, the gyroscope performance is stable. But, allowing  $V_{AC}$  to surpass particular value, the structural restoring force cannot resist the electrodynamic attraction and the beam becomes unstable.

The influence of the length-scale and nonlocal parameters on the time response of the gyroscope in its stable regime is displayed in Fig. 9. Part (a) of the figure shows that by increasing the effect of nonlocality, the velocity amplitude in the sense direction declines while deflection  $v(t)$  get increased. On the other hand, as spotlighted in part (b), while the length-scale parameter raises up, the amplitude of deflection and velocity along the sense direction further restricted. This implies that taking advantage of materials with higher  $l_m$  values in design and construction of microgyroscopes can effectively reduce the operational limit of the system and diminish the possibility of pull-in occurrence.

The temporal response of the gyroscope in the verge of instability are plotted in Fig. 10 for different nonlocal and length-scale values. According to this figure, for a constant combination of DC and AC loading, the beam can operate in stable region for some small values of  $ea$  and  $l_m$ . Nonetheless, by increasing the nonlocal and/or

**Fig. 5** Normalized time domain response of the gyroscope in the sense and drive directions



decreasing the length-scale variables while keeping DC and AC voltages unchanged, the system loses its stability and continues its motion until it collapses onto the fixed electrode.

## 5.2 Frequency Response

In this section, the frequency responses of the gyroscope along the sense and drive directions in the vicinity of fundamental natural frequency of the system are studied. In order to analyze the role of nonlocal and length-scale parameters on the frequency response, the previously described gyroscope (Table 1) is considered and  $V_{DC} = 8V$ ,  $V_{AC} = 0.1V$ ,  $\hat{\Omega} = 100$  rad/s and  $\hat{\Omega} = 0$  is adopted throughout the section.

Figures 11 and 12 present the frequency response along the sense and drive directions respectively, for different  $ea$  values. Using the data provided in these figures, the following inferences can be resulted:

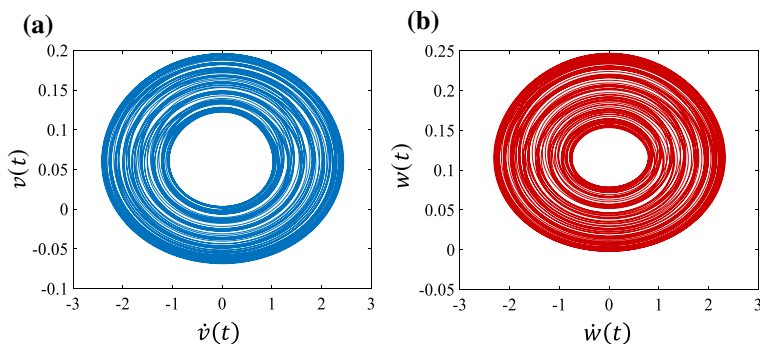
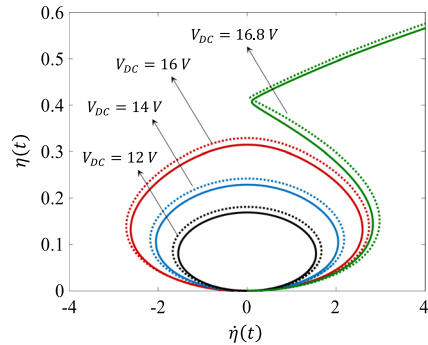


**Fig. 6** Representation of limit cycle along: **a** sense and **b** drive directions under combined AC-CD loading



**Fig. 7** Phase diagram corresponds to the electrodynamic performance of the gyroscope for different DC voltages with solid and dashed lines represent the response in sense and drive directions respectively (with  $V_{AC} = 0.5V$ ,  $I_m = 0.01L$  and  $ea = 0.2$ )

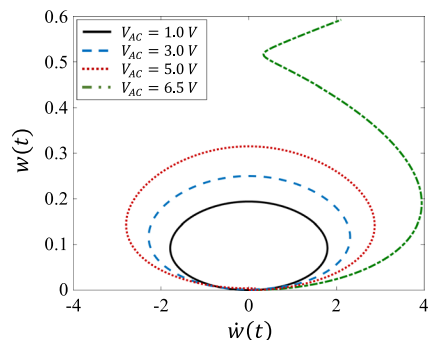


- Harmonic excitation in the drive direction engenders similar response in the sense direction due to gyroscopic effect of the Coriolis force.
- In excitation frequencies away enough from the fundamental frequency, the more the nonlocal parameter values, the more the amplitude of vibration.
- Near the fundamental frequency of the system, the influence of  $ea$  is reverse. As Figs. 11 and 12 demonstrate, in these areas smaller  $ea$  values leads to lower vibration amplitudes.
- By increasing the nonlocal parameter, the dynamic amplification takes place in smaller excitation frequencies. More specifically, by increasing the value of  $ea$ , both peaks of the diagram are shifted toward smaller frequency values. As a consequence, the nonlocal variable plays a dual role in the frequency response of the system which should be carefully considered in design procedure.

The dependence of the frequency response on the length-scale parameters is also characterized in Figs. 13 and 14. According to these figures:

- The amplitude of vibration is reduced by increasing the length-scale parameter. This fact is true both for excitation frequencies away from and near the gyroscope fundamental frequency.

**Fig. 8** Phase diagram corresponds to the electrodynamic performance of the gyroscope in the drive direction for different AC voltages (with  $V_{DC} = 12V$ ,  $I_m = 0.01L$  and  $ea = 0.2$ )



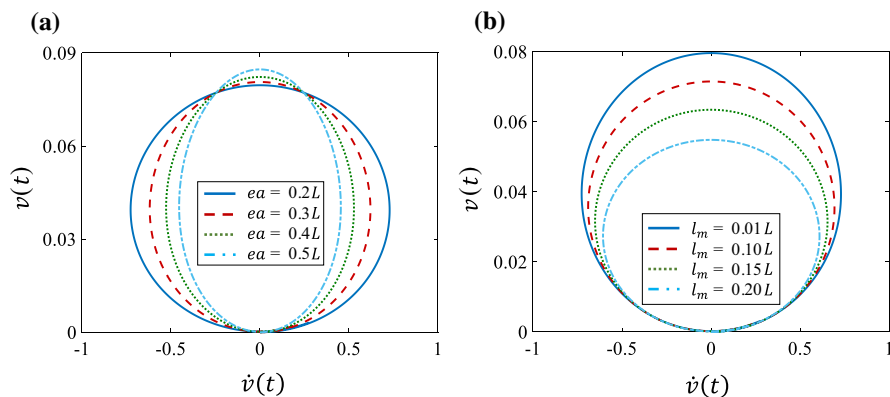


**Fig. 9** Phase diagram corresponds to the stable motion along the sense direction with  $V_{DC} = 10V$  and  $V_{AC} = 0.5V$ : **a** the significance of nonlocal parameter  $ea$  for  $l_m = 0.01L$ ; **b** the significance of length-scale parameter  $l_m$  for  $ea = 0.2$

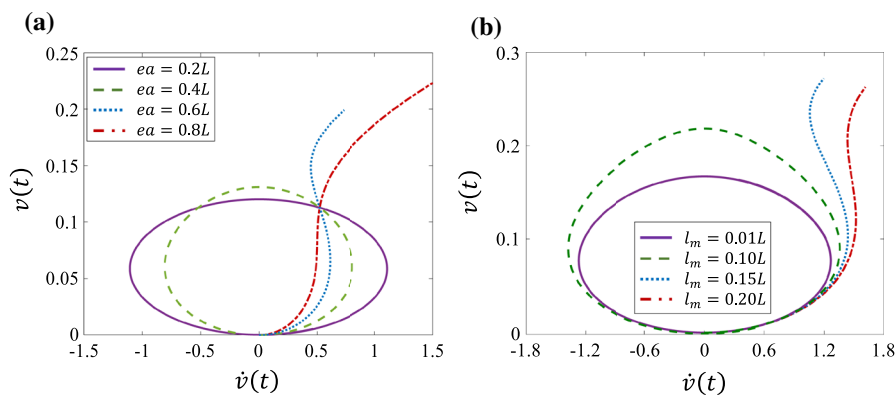


**Fig. 10** Phase diagram corresponds to the unstable motion along the sense direction  $V_{AC} = 0.5V$ : **a** the significance of nonlocal parameter  $ea$  for  $l_m = 0.01L$  and  $V_{DC} = 10V$ ; **b** the significance of length-scale parameter  $lm$  for  $ea = 0.4$  and  $V_{DC} = 14V$

- Near the fundamental frequency, as  $l_m$  increases, the maximum amplitude along the sense and drive directions become smaller and the dynamic amplification occurs in higher frequencies. Furthermore, the two amplification frequencies become closer.

**Fig. 11** Near resonance frequency response of the microgyroscope in the sense direction for different nonlocal parameters

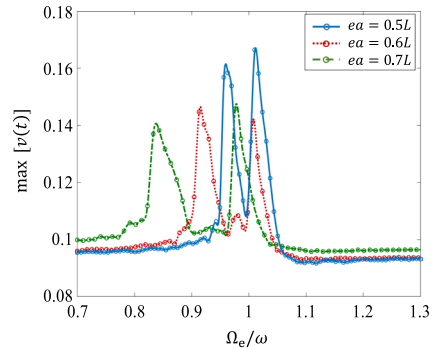
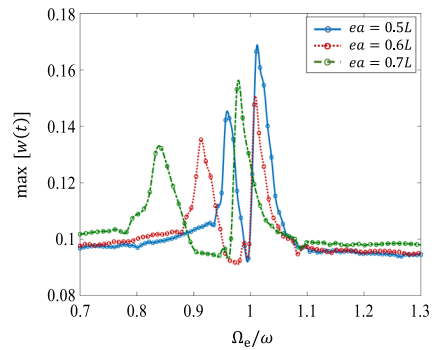


**Fig. 12** Near resonance frequency response of the microgyroscope in the drive direction for different nonlocal parameters



## 6 Conclusions

In this paper, a nonlocal strain gradient formulation for doubly clamped microgyroscopes was developed to simultaneously incorporate the effects of nonlocal and gradient strains into the mathematical model in order to improve the accuracy of mathematical predictions. The governing equations corresponding to the lateral vibration of the microgyroscope along the sense and drive directions as well as the associated boundary conditions were developed employing energy approach which were then used to derive a reduced-order model for the system. By investigating the electrostatic behavior of the gyroscope, it was demonstrated that the maximum static deflection and maximum allowable voltage are affected by the values of higher-order variables. In better words, for smaller values of nonlocal parameter  $ea$  or higher values of the length-scale parameter  $l_m$ , pull-in instability occurs at higher voltage values and the stable operating ranger would be broader. Temporal response of the gyroscope is then obtained by solving the dynamic reduced order model. It was demonstrated that the microgyroscope has a stable limit cycle in both sense and drive directions, but by increasing the DC or AC voltages beyond specific values, the gyroscope response become unstable. Furthermore, stability of the gyroscope was shown to be subjected to the nonlocal and length-scale parameters so that increasing the length-scale or nonlocal values can increase the

**Fig. 13** Near resonance frequency response of the microgyroscope in the sense direction for different length-scale parameters

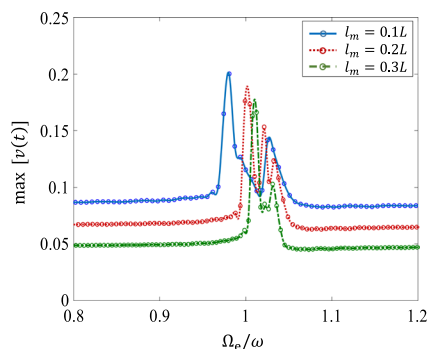
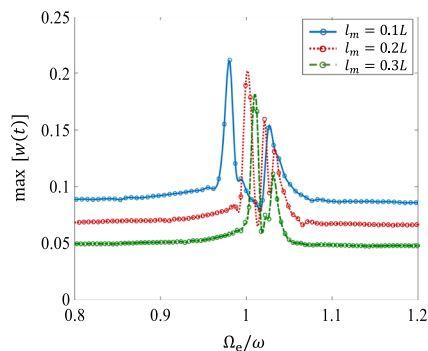


**Fig. 14** Near resonance frequency response of the microgyroscope in the drive direction for different length-scale parameters



amplitude of gyroscope response and finally leads to instability of the system. Finally, the gyroscope frequency responses were presented and the role of nonlocal and length-scale parameters were investigated. As the results of this section clarified, these two important design parameters can have different impacts near and away from the gyroscope fundamental frequency. The maximum amplitude near resonance is increased by decreasing  $ea$  and/or  $l_m$  values. Furthermore, the frequency corresponds to the maximum amplitude approaches the fundamental frequency of the gyroscope by decreasing  $ea$  or increasing the  $l_m$  values. The results of this study can be employed to design and tune microgyroscopes for operating within a desirable stable range or satisfying specific dynamic performance.

## Appendix I: Boundary Conditions

$$\delta \hat{u} = 0 \quad \text{or} \quad N_c = 0 \quad (\text{I-1})$$

$$\delta \left( \frac{\partial \hat{u}}{\partial \hat{x}} \right) = 0 \quad \text{or} \quad N_{nc} = 0 \quad (\text{I-2})$$

$$\delta \hat{w} = 0 \quad \text{or} \quad N_c \frac{\partial \hat{w}}{\partial \hat{x}} + \frac{\partial M_c^{(z)}}{\partial \hat{x}} = 0 \quad (\text{I-3})$$

$$\delta \left( \frac{\partial \hat{w}}{\partial \hat{x}} \right) = 0 \quad \text{or} \quad N_{nc} \frac{\partial \hat{w}}{\partial \hat{x}} - M_c^{(z)} = 0 \quad (\text{I-4})$$

$$\delta \left( \frac{\partial^2 \hat{w}}{\partial \hat{x}^2} \right) = 0 \quad \text{or} \quad M_{nc}^{(z)} = 0 \quad (\text{I-5})$$

$$\delta \hat{v} = 0 \quad \text{or} \quad N_c \frac{\partial \hat{v}}{\partial \hat{x}} + \frac{\partial M_c^{(y)}}{\partial \hat{x}} = 0 \quad (\text{I-6})$$

$$\delta \left( \frac{\partial \hat{v}}{\partial \hat{x}} \right) = 0 \quad \text{or} \quad N_{nc} \frac{\partial \hat{v}}{\partial \hat{x}} - M_c^{(y)} = 0 \quad (\text{I-7})$$

$$\delta \left( \frac{\partial^2 \hat{v}}{\partial \hat{x}^2} \right) = 0 \quad \text{or} \quad M_{nc}^{(y)} = 0 \quad (\text{I-8})$$

**Acknowledgements** The authors wish to express appreciation to Research Deputy of Ferdowsi University of Mashhad for supporting this project by Grant No. 46414-18/01/97.

## Compliance with Ethical Standards

**Conflict of interest** The authors declare that they have no conflict of interest.

## References

1. Karpenko, A., Jacobs, D., Baek, J., & Levoy, M. (2011). Digital video stabilization and rolling shutter correction using gyroscopes. *CSTR*, 1, 2.
2. Ojeda, L., Chung, H., & Borenstein, J. (2000). Precision calibration of fiber-optics gyroscopes for mobile robot navigation. In: *Robotics and automation, 2000, proceedings. ICRA'00, IEEE international conference on* (Vol. 3, pp. 2064–2069). IEEE.
3. Acar, C., Schofield, A. R., Trusov, A. A., Costlow, L. E., & Shkel, A. M. (2009). Environmentally robust MEMS vibratory gyroscopes for automotive applications. *IEEE Sensors Journal*, 9(12), 1895–1906.
4. Delporte, B., Perrotton, L., Grandpierre, T., & Trichet, J. (2012). Accelerometer and magnetometer based gyroscope emulation on smart sensor for a virtual reality application. *Sensor and Transducers Journal*, 14(Special Issue ISSN 1726-5479), 32–47.
5. Rocon, E., Moreno, J., Ruiz, A., Brunetti, F., Miranda, J., & Pons, J. (2007). Application of inertial sensors in rehabilitation robotics. In: *Rehabilitation robotics, 2007, ICORR 2007, IEEE 10th International Conference on* (pp. 145–150). IEEE.
6. Priyanka, E.B., Thangavel, S., & Gao, X.-Z. (2020). Review analysis on cloud computing based smart grid technology in the oil pipeline sensor network system. *Petroleum Research*. <https://doi.org/10.1016/j.ptlrs.2020.10.001>

7. Priyanka, E., Thangavel, S., & Pratheep, V. (2020). Enhanced digital synthesized phase locked loop with high frequency compensation and clock generation. *Sensing and Imaging*, 21(1), 1–12.
8. Bhaskaran, P. E., Chennippan, M., & Subramaniam, T. (2020). Future prediction & estimation of faults occurrences in oil pipelines by using data clustering with time series forecasting. *Journal of Loss Prevention in the Process Industries*, 66, 104203.
9. Priyanka, E., Maheswari, C., Ponnibala, M., & Thangavel, S. (2019). SCADA based remote monitoring and control of pressure & flow in fluid transport system using IMC-PID controller. *Advances in Systems Science and Applications*, 19(3), 140–162.
10. Bhaskaran, P. E., Maheswari, C., Thangavel, S., Ponnibala, M., Kalavathidevi, T., & Sivakumar, N. (2020). IoT Based monitoring and control of fluid transportation using machine learning. *Computers & Electrical Engineering*, 89, 106899.
11. Mojahedi, M., Moeenfar, H., & Ahmadian, M. T. (2009). A new efficient approach for modeling and simulation of nano-switches under the combined effects of intermolecular surface forces and electrostatic actuation. *International Journal of Applied Mechanics*, 1(02), 349–365.
12. Abdel-Rahman, E. M., Younis, M. I., & Nayfeh, A. H. (2002). Characterization of the mechanical behavior of an electrically actuated microbeam. *Journal of Micromechanics and Microengineering*, 12(6), 759.
13. Kuang, J.-H., & Chen, C.-J. (2004). Dynamic characteristics of shaped micro-actuators solved using the differential quadrature method. *Journal of Micromechanics and Microengineering*, 14(4), 647.
14. Rasekh, M., & Khadem, S. (2011). Pull-in analysis of an electrostatically actuated nano-cantilever beam with nonlinearity in curvature and inertia. *International Journal of Mechanical Sciences*, 53(2), 108–115.
15. Nayfeh, A. H., Younis, M. I., & Abdel-Rahman, E. M. (2007). Dynamic pull-in phenomenon in MEMS resonators. *Nonlinear Dynamics*, 48(1–2), 153–163.
16. Krylov, S. (2007). Lyapunov exponents as a criterion for the dynamic pull-in instability of electrostatically actuated microstructures. *International Journal of Non-Linear Mechanics*, 42(4), 626–642.
17. Rahaeifard, M., Kahrobaiyan, M., Ahmadian, M., & Firoozbakhsh, K. (2012). Size-dependent pull-in phenomena in nonlinear microbridges. *International Journal of Mechanical Sciences*, 54(1), 306–310.
18. Shen, J., Wang, H., & Zheng, S. (2018). Size-dependent pull-in analysis of a composite laminated micro-beam actuated by electrostatic and piezoelectric forces: Generalized differential quadrature method. *International Journal of Mechanical Sciences*, 135, 353–361.
19. Farokhi, H., & Ghayesh, M. H. (2016). Size-dependent behaviour of electrically actuated microcantilever-based MEMS. *International Journal of Mechanics and Materials in Design*, 12(3), 301–315.
20. Rezazadeh, G., Fathalilou, M., & Sadeghi, M. (2011). Pull-in voltage of electrostatically-actuated microbeams in terms of lumped model pull-in voltage using novel design corrective coefficients. *Sensing and Imaging: An International Journal*, 12(3–4), 117–131.
21. Kivi, A. R., Azizi, S., & Marzbanrad, J. (2015). Investigation of static and dynamic pull-in instability in a FGP micro-beam. *Sensing and Imaging*, 16(1), 2.
22. Nan, C.-W., & Clarke, D. (1996). The influence of particle size and particle fracture on the elastic/plastic deformation of metal matrix composites. *Acta Materialia*, 44(9), 3801–3811.
23. Eringen, A. C., & Edelen, D. (1972). On nonlocal elasticity. *International Journal of Engineering Science*, 10(3), 233–248.
24. Eringen, A. C. (1983). On differential equations of nonlocal elasticity and solutions of screw dislocation and surface waves. *Journal of applied physics*, 54(9), 4703–4710.
25. Reddy, J., & El-Borgi, S. (2014). Eringen's nonlocal theories of beams accounting for moderate rotations. *International Journal of Engineering Science*, 82, 159–177.
26. Rahmani, O., & Pedram, O. (2014). Analysis and modeling the size effect on vibration of functionally graded nanobeams based on nonlocal Timoshenko beam theory. *International Journal of Engineering Science*, 77, 55–70.
27. Najaf, F., El-Borgi, S., Reddy, J., & Mrabet, K. (2015). Nonlinear nonlocal analysis of electrostatic nanoactuators. *Composite Structures*, 120, 117–128.
28. Kivi, A. R., Azizi, S., & Norouzi, P. (2017). Bifurcation analysis of an electrostatically actuated nano-beam based on modified couple stress theory. *Sensing and Imaging*, 18(1), 32.
29. Ebrahimi, F., & Salari, E. (2015). Thermo-mechanical vibration analysis of nonlocal temperature-dependent FG nanobeams with various boundary conditions. *Composites Part B: Engineering*, 78, 272–290.

30. Ebrahimi, F., & Salari, E. (2015). Nonlocal thermo-mechanical vibration analysis of functionally graded nanobeams in thermal environment. *Acta Astronautica*, 113, 29–50.
31. Nejad, M. Z., Hadi, A., & Rastgoo, A. (2016). Buckling analysis of arbitrary two-directional functionally graded Euler–Bernoulli nano-beams based on nonlocal elasticity theory. *International Journal of Engineering Science*, 103, 1–10.
32. Ansari, R., Oskouie, M. F., Gholami, R., & Sadeghi, F. (2016). Thermo-electro-mechanical vibration of postbuckled piezoelectric Timoshenko nanobeams based on the nonlocal elasticity theory. *Composites Part B: Engineering*, 89, 316–327.
33. Mindlin, R., & Tiersten, H. (1962). Effects of couple-stresses in linear elasticity. *Archive for Rational Mechanics and analysis*, 11(1), 415–448.
34. Aifantis, E. C. (1992). On the role of gradients in the localization of deformation and fracture. *International Journal of Engineering Science*, 30(10), 1279–1299.
35. Toupin, R. A. (1962). Elastic materials with couple-stresses. *Archive for Rational Mechanics and Analysis*, 11(1), 385–414.
36. Lam, D. C., Yang, F., Chong, A., Wang, J., & Tong, P. (2003). Experiments and theory in strain gradient elasticity. *Journal of the Mechanics and Physics of Solids*, 51(8), 1477–1508.
37. Kahrobaian, M., Rahaeifard, M., Tajalli, S., & Ahmadian, M. (2012). A strain gradient functionally graded Euler–Bernoulli beam formulation. *International Journal of Engineering Science*, 52, 65–76.
38. Ghayesh, M. H., Amabili, M., & Farokhi, H. (2013). Nonlinear forced vibrations of a microbeam based on the strain gradient elasticity theory. *International Journal of Engineering Science*, 63, 52–60.
39. Akgöz, B., & Civalek, Ö. (2013). A size-dependent shear deformation beam model based on the strain gradient elasticity theory. *International Journal of Engineering Science*, 70, 1–14.
40. Farokhi, H., Ghayesh, M. H., Kosasih, B., & Akaber, P. (2016). On the nonlinear resonant dynamics of Timoshenko microbeams: Effects of axial load and geometric imperfection. *Meccanica*, 51(1), 155–169.
41. Radgolchin, M., & Moeenfar, H. (2018). An analytical approach for modeling nonlinear vibration of doubly clamped functionally graded Timoshenko microbeams using strain gradient theory. *International Journal of Dynamics and Control*, 6(3), 990–1007.
42. Ghayesh, M. H., Farokhi, H., Hussain, S., Gholipour, A., & Arjomandi, M. (2017). A size-dependent nonlinear third-order shear-deformable dynamic model for a microplate on an elastic medium. *Microsystem Technologies*, 23(8), 3281–3299.
43. Wang, B., Liu, M., Zhao, J., & Zhou, S. (2014). A size-dependent Reddy–Levinson beam model based on a strain gradient elasticity theory. *Meccanica*, 49(6), 1427–1441.
44. Ghayesh, M. H., & Farokhi, H. (2018). Size-dependent internal resonances and modal interactions in nonlinear dynamics of microcantilevers. *International Journal of Mechanics and Materials in Design*, 14(1), 127–140.
45. Radgolchin, M., & Moeenfar, H. (2018). Size-dependent nonlinear vibration analysis of shear deformable microarches using strain gradient theory. *Acta Mechanica*, 229(7), 3025–3049.
46. Raahemifar, K. (2017). Size-dependent asymmetric buckling of initially curved shallow nano-beam using strain gradient elasticity. *Microsystem Technologies*, 23(10), 4567–4578.
47. Akgöz, B., & Civalek, Ö. (2015). Bending analysis of FG microbeams resting on Winkler elastic foundation via strain gradient elasticity. *Composite Structures*, 134, 294–301.
48. Lei, J., He, Y., Zhang, B., Gan, Z., & Zeng, P. (2013). Bending and vibration of functionally graded sinusoidal microbeams based on the strain gradient elasticity theory. *International Journal of Engineering Science*, 72, 36–52.
49. Zhang, J., & Fu, Y. (2012). Pull-in analysis of electrically actuated viscoelastic microbeams based on a modified couple stress theory. *Meccanica*, 47(7), 1649–1658.
50. Attia, M. A. (2017). Investigation of size-dependent quasistatic response of electrically actuated nonlinear viscoelastic microcantilevers and microbridges. *Meccanica*, 52(10), 2391–2420.
51. Li, Y., Feng, W., & Cai, Z. (2014). Bending and free vibration of functionally graded piezoelectric beam based on modified strain gradient theory. *Composite Structures*, 115, 41–50.

52. Ghorbanpour-Arani, A., Rastgoo, A., Sharafi, M., Kolahchi, R., & Arani, A. G. (2016). Nonlocal viscoelasticity based vibration of double viscoelastic piezoelectric nanobeam systems. *Meccanica*, 51(1), 25–40.
53. Zheng, Y., Chen, T., & Chen, C. (2017). A size-dependent model to study nonlinear static behavior of piezoelectric cantilever microbeams with damage. *Microsystem Technologies*, 23(10), 4679–4686.
54. Mokhtari, A., Sarvestan, V., & Mirdamadi, H. R. (2017). Thermal and tensile loading effects on size-dependent vibration response of traveling nanobeam by wavelet-based spectral element modeling. *Meccanica*, 52(9), 2169–2187.
55. Li, Z., He, Y., Lei, J., Han, S., Guo, S., & Liu, D. (2019). Experimental investigation on size-dependent higher-mode vibration of cantilever microbeams. *Microsystem Technologies*, 25(8), 3005–3015.
56. Akgöz, B., & Civalek, Ö. (2013). Buckling analysis of functionally graded microbeams based on the strain gradient theory. *Acta Mechanica*, 224(9), 2185–2201.
57. Ansari, R., Gholami, R., Shojaei, M. F., Mohammadi, V., & Sahmani, S. (2013). Size-dependent bending, buckling and free vibration of functionally graded Timoshenko microbeams based on the most general strain gradient theory. *Composite Structures*, 100, 385–397.
58. Pradiptya, I., & Ouakad, H. M. (2018). Size-dependent behavior of slacked carbon nanotube actuator based on the higher-order strain gradient theory. *International Journal of Mechanics and Materials in Design*, 14(3), 393–415.
59. Sedighi, H. M. (2014). Size-dependent dynamic pull-in instability of vibrating electrically actuated microbeams based on the strain gradient elasticity theory. *Acta Astronautica*, 95, 111–123.
60. Radgolchin, M., & Moeenfar, H. (2018). Size-dependent piezoelectric energy-harvesting analysis of micro/nano bridges subjected to random ambient excitations. *Smart Materials and Structures*, 27(2), 025015.
61. Reddy, J., & Pang, S. (2008). Nonlocal continuum theories of beams for the analysis of carbon nanotubes. *Journal of Applied Physics*, 103(2), 023511.
62. Lim, C., & Wang, C. (2007). Exact variational nonlocal stress modeling with asymptotic higher-order strain gradients for nanobeams. *Journal of Applied Physics*, 101(5), 054312.
63. Fleck, N., & Hutchinson, J. (1993). A phenomenological theory for strain gradient effects in plasticity. *Journal of the Mechanics and Physics of Solids*, 41(12), 1825–1857.
64. Kahrobaiyan, M., Asghari, M., Rahaeifard, M., & Ahmadian, M. (2011). A nonlinear strain gradient beam formulation. *International Journal of Engineering Science*, 49(11), 1256–1267.
65. Lim, C., Zhang, G., & Reddy, J. (2015). A higher-order nonlocal elasticity and strain gradient theory and its applications in wave propagation. *Journal of the Mechanics and Physics of Solids*, 78, 298–313.
66. Li, L., & Hu, Y. (2015). Buckling analysis of size-dependent nonlinear beams based on a nonlocal strain gradient theory. *International Journal of Engineering Science*, 97, 84–94.
67. Şimşek, M. (2016). Nonlinear free vibration of a functionally graded nanobeam using nonlocal strain gradient theory and a novel Hamiltonian approach. *International Journal of Engineering Science*, 105, 12–27.
68. Li, L., & Hu, Y. (2016). Nonlinear bending and free vibration analyses of nonlocal strain gradient beams made of functionally graded material. *International Journal of Engineering Science*, 107, 77–97.
69. Fang, J., Gu, J., & Wang, H. (2018). Size-dependent three-dimensional free vibration of rotating functionally graded microbeams based on a modified couple stress theory. *International Journal of Mechanical Sciences*, 136, 188–199.
70. Li, L., Hu, Y., & Li, X. (2016). Longitudinal vibration of size-dependent rods via nonlocal strain gradient theory. *International Journal of Mechanical Sciences*, 115, 135–144.
71. Ebrahimi, F., & Barati, M. R. (2017). A nonlocal strain gradient refined beam model for buckling analysis of size-dependent shear-deformable curved FG nanobeams. *Composite Structures*, 159, 174–182.
72. Xu, X.-J., Wang, X.-C., Zheng, M.-L., & Ma, Z. (2017). Bending and buckling of nonlocal strain gradient elastic beams. *Composite Structures*, 160, 366–377.
73. Farajpour, A., Yazdi, M. H., Rastgoo, A., & Mohammadi, M. (2016). A higher-order nonlocal strain gradient plate model for buckling of orthotropic nanoplates in thermal environment. *Acta Mechanica*, 227(7), 1849–1867.



74. Mojahedi, M., & Rahaeifard, M. (2016). A size-dependent model for coupled 3D deformations of nonlinear microbridges. *International Journal of Engineering Science*, 100, 171–182.
75. Rao, S. S. (2007). *Vibration of continuous systems*. New York: Wiley.
76. Radgolchin, M., & Moeenfar, H. (2018). Development of a multi-level adaptive fuzzy controller for beyond pull-in stabilization of electrostatically actuated microplates. *Journal of Vibration and Control*, 24(5), 860–878.
77. Radgolchin, M., & Moeenfar, H. (2018). Analytical modeling of nonlinear flexural-extensional vibration of flexure beams with an interconnected compliant element. *Mechanics Research Communications*, 89, 23–33.
78. Gutschmidt, S. (2010) The influence of higher-order mode shapes for reduced-order models of electrostatically actuated microbeams. *Journal of Applied Mechanics*, 77(4), 45–68.

**Publisher's Note** Springer Nature remains neutral with regard to jurisdictional claims in published maps and institutional affiliations.